Investigation of wave characteristics in a semi-enclosed bay based on SWAN model validated with buoys and ADP-observed currents*

LU Jing[1, 2], TENG Yong[1, 2, **], CHI Wanqing[1], YIN Liping[1, 2], WANG Daolong[1, 2]

[1] First Institute of Oceanography, MNR, Qingdao 266061, China

[2] Laboratory for Regional Oceanography and Numerical Modeling, Qingdao National Laboratory for Marine Science and Technology, Qingdao 266237, China

Abstract   In this study, the simulating waves nearshore (SWAN) model with a locally refined curvilinear grid system was constructed to simulate waves in Jervis Bay and the neighbouring ocean of Australia, with the aim of examining the wave characteristics in an area with special topography and practical importance. This model was verified by field observations from buoys and acoustic Doppler profilers (ADPs). The model precisions were validated for both wind-generated waves and open-ocean swells. We present an approach with which to convert ADP-observed current data from near the bottom into the significant wave height. Our approach is deduced from the Fourier transform technique and the linear wave theory. The results illustrate that the location of the bay entrance is important because it allows the swells in the dominant direction to propagate into the bay despite the narrowness of the bay entrance. The wave period T_p is also strongly related to the wave direction in the semi-enclosed bay. The T_p is great enough along the entire propagating direction from the bay entrance to the top of the bay, and the largest T_p appears along the north-west coast, which is the end tip of the swells' propagation.

Keyword: wave; simulating waves nearshore (SWAN); acoustic Doppler profilers (ADPs); buoy; swell; semi-enclosed bay

1 INTRODUCTION

Semi-enclosed bays are usually protected from large waves. The study region of Jervis Bay (JB) is a semi-enclosed embayment on the south-east coast of Australia, and the bay's entrance is located on its south-east. The coastline (which runs north-east to south-west) and the bay entrance both face the open ocean from the south-east (Fig.1b). The trade wind is also mainly south-easterly from the open ocean. These factors make JB a special study area.
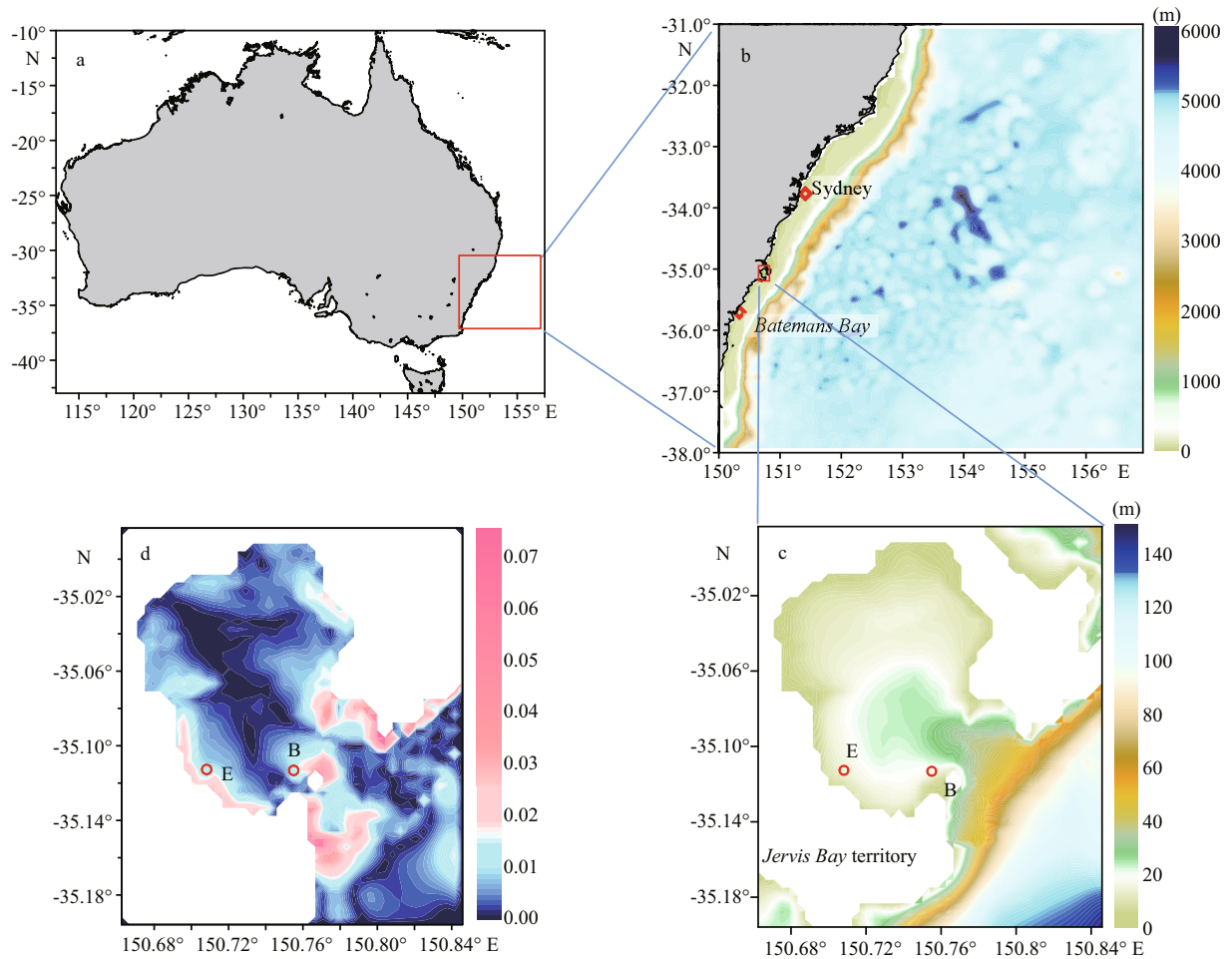
JB has an area of 102 km² (16 km from south to north and 10 km from west to east). JB is an entrance to the ocean, surrounded by New South Wales and by the Australian Capital Territory. (The Australian Navy base, HMAS Creswell, is in the JB Territory, a part of the Australian Capital Territory). Therefore, JB is important not only for commercial requirements but also because the Royal Australian Navy uses its natural harbour. Waves play a key role in coastal dynamics, but few studies of the waves in JB have been published since Wright (1976) estimated the role of shallow water modification and frictional

Fig.1 Australian coastline (a); model domain, overlaying topography (metres) (b). Buoys in Batemans Bay and Sydney are marked with red diamonds; ADP observation sites B and E marked with red circles, overlying the topography of Jervis Bay (JB) (c); bottom slope of JB (d)

dissipation on the coastal wave regime from Sydney to JB by analysing the Botany Bay offshore wave rider. In addition, previous studies have not modelled the surface wave characteristics in JB and its relationship with the location of the bay entrance.

In this study, we first deduced a method to derive the wave height from the currents observed by bottom-mounted acoustic Doppler profilers (ADPs). The measured currents were used to extract waves according to the Fourier transform technique during a period of moderate wind speeds.

Acoustic observation is an ordinary method to measure waves. Marine radar was used decades ago to discern the wave spectrum from the radar backscatter from the sea (Chen et al., 2015a, b). Unlike remote sensing, acoustic Doppler instruments have been proved an effective method to observe waves in situ. Unlike buoys, acoustic Doppler current profilers (ADCPs) and ADPs can measure waves and currents simultaneously. Considerable attention has

been devoted to explore its role in measuring waves since Pinkel and Smith (1987) first provided a high-quality measurement of wave direction with horizontally projected Doppler sonar beams. Rorbaek and Andersen (2002) obtained wave measurements with an ADCP and compared them with those from a heave/pitch/roll buoy due to different measurement principles. Strong et al. (2000) used an ADCP to determine the wave height and direction in coastal-depth waters. It has been shown that the directional spectra obtained from an ADCP are sharper than those from point measurements, and an ADCP can resolve complex multi-directional wave distributions. Churchill et al. (2006) partitioned directional wave spectra derived from ADCP measurements south of Martha's Vineyard to separate the wind waves from the incoming swells.

High-frequency currents have often been used to derive wave spectra. Siadatmousavi et al. (2012) deployed a downward-looking SonTek 1.5 MHz PC-

Table 1 Definition of variables

Wave departures at height Z	s_Z	Frequency	f
Surface elevation	η	Dimensionless peak frequency f_m	$\tilde{f}_m$
Significant wave height	H_s	Zero-th moment of variance spectrum	m_0
Current spectrum	$P(\sigma)$	Dimensionless variance m; m is integrated from wave spectrum	$\tilde{m}$
Wave spectrum	$S(\sigma)$	Wave potential	ϕ
Radian frequency	σ	Wave number	k

ADP to record velocity profiles at 2 Hz near the bottom over the muddy Atchafalaya shelf. The PC-ADP measured wave spectra near the bottom and gathered bottom boundary layer data. Siadatmousavi and Jose (2015) computed directional wave spectra from ADCP data using WavesMon software, and bimodal wave frequency spectra were observed during a winter storm in the northern Gulf of Mexico. However, ADPs/ADCPs are usually bottom-mounted, so a method to precisely convert currents into surface wave height becomes an important problem because it is difficult for a bottom-mounted ADP to measure surface waves. The approach of conversion from the bottom to the surface has seldom been discussed.

In this paper, we measured high-frequency currents from ADPs and converted the measurements in the near-bottom layer to the surface layer via a deduced method based on linear wave theory. A simulating waves nearshore (SWAN) model with locally refined grids was constructed to simulate waves in JB and the surrounding area. It was then calibrated with the wave data derived from ADP-observed currents. The buoy data during strong winds were also used to verify the ability to simulate wind-generated waves. Finally, the characteristics of the surface waves were investigated based on the SWAN simulation results.

2 METHOD

2.1 Process of deriving significant wave height from ADP-observed currents

High-frequency current data from ADPs were used to analyse wave characteristics. ADPs can effectively obtain estimates of wave spectra. They are generally bottom-mounted, so the bottom currents must be converted to the wave height at the surface to calibrate the modelled wave height. In this study, we converted the measurements near the bottom to surface characteristics with an analytical method based on the Fourier transform technique and linear wave theory. The steps for transformation of the bottom

measurements are presented below in detail. For simplification, the definitions for the variables used are listed in Table 1.

First, we obtain the current spectrum $P(\sigma)$ from the high-frequency currents from the ADPs using Fourier transform. We then converted the current spectrum $P(\sigma)$ to a wave spectrum $S(\sigma)$ as,

$$P(\sigma)=P(f)/2\pi, \quad (1)$$

$$S(\sigma)=\sigma^{-2}P(\sigma), \quad (2)$$

where σ represents the radian frequency, $\sigma=2\pi/T$. We obtained the wave departures s_Z at the reference height Z near the bottom from the wave spectrum. We then take the integral of the wave spectrum to obtain the variance m_0 as in Eq.3.

$$m_0=\int S(\sigma)d\sigma, \quad (3)$$

$$s_Z = 4\sqrt{m_0}. \quad (4)$$

The wave departures s_Z can be calculated with m_0 according to Eq.4.

For the last step, we transformed s_Z from near the bottom to the surface elevation η. The expression for wave departures s_Z is based on the work of Mellor (2013) and given as,

$$s_Z=aF_{ss}\cos\psi=F_{ss}\eta. \quad (5)$$

Here, coefficient $F_{ss}=[\sinh k(h+z)]/\sinh kh$. Here, ψ represents $\psi=kx-\sigma t$. At last, H_{m_0} can be obtained as

$$H_{m_0} = 2\eta = 2s_Z \frac{\sinh kh}{\sinh k(h+z)}. \quad (6)$$

The detail to deduce Eq.5 is shown in the Appendix.

2.2 Description and setting of SWAN model

The SWAN model was developed for shallow waters by Delft University of Technology (Komen et al., 1984; Booij et al., 1999; SWAN Team, 2014) and is known as a third-generation phase-averaged model. A SWAN model was successfully set up for the wave conditions in semi-enclosed domains (Signell et al., 2005; Pallares et al., 2014). Waves in the SWAN model are described by the two-dimensional wave
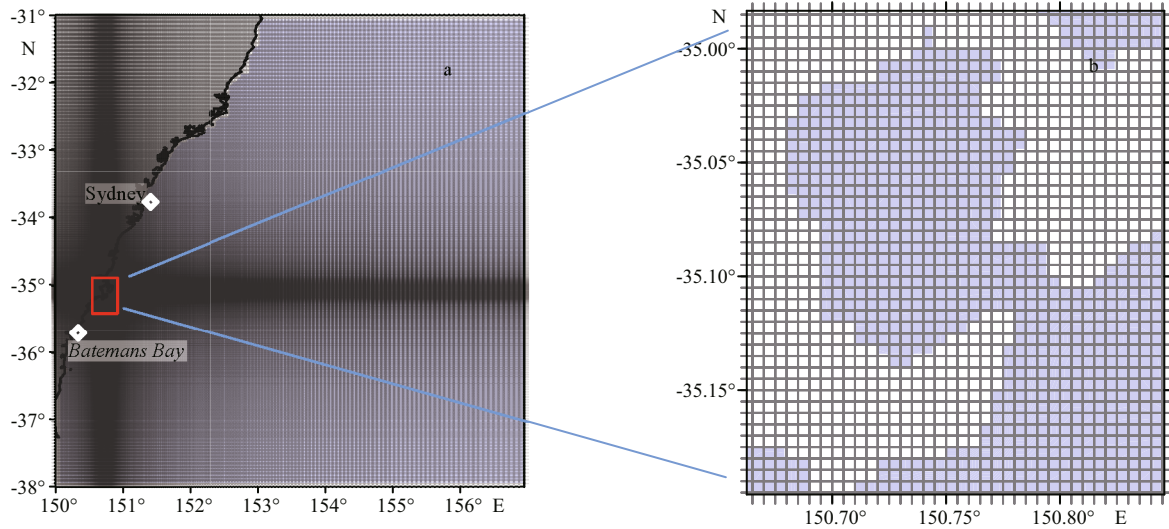
Fig.2 Grid distribution with locally fine resolution in JB

a. model domain; b. JB.

action density spectrum. The evolution of the wave spectrum is described by the radiative transfer equation:

$$\frac{\partial N}{\partial t} + \nabla \cdot cN = \frac{S_{tot}}{\sigma} = \frac{S_{in} + S_{ds} + S_{nl} + S_{bot} + S_{db} + S_{tr}}{\sigma} , \quad (7)$$

where $N=(\sigma, \theta, x, t)$ is the wave action density spectrum dependent upon the radian frequency $\sigma = 2\pi f$ from a frame of reference relative to any local currents; the wave direction is θ; c is the energy propagation velocity; S_{tot} represents all energy fluxes that contribute to the wind-wave evolution; and the action density is related to the energy density as simply $N=E/\sigma$. The balance equation of the SWAN model considers the local rate of change in time, the propagation in geographical space, the shifting of the relative frequency due to variations in depths and currents and the depth-induced and current-induced refraction. In finite depths, additional terms from the bottom-friction S_{bot}, depth-induced breaking S_{db} and triad interactions S_{tr} become significant. These source terms are all spectral functions. In this study, 36 uniformly distributed directions were used, with 24 geometrically distributed frequencies. The min value fmin is 0.05 Hz, and fmax is 1 Hz. The model time step was 3 minutes.

The model domain is in the south-eastern part of Australia from 150.0°E to 156.95°E longitude and from 37.95°S to 31.045°S latitude (Fig.1b). Most of the model domain is in deep ocean with a depth greater than 4 000 m. The isobath is intensive near the coast line, and the continental shelf is relatively narrow. The isobaths in JB decrease from the south-east entrance to the northern top of the bay, as seen from Fig.1c. JB is less than 40 m deep, and the depth at the middle of the bay is roughly 20 m. Figure 2 describes the curvilinear grid system that is refined in JB locally. It has 234 × 258 horizontal grids in the x and y directions, with finer grids on the periphery of JB (x: 438 to 7 403 m; y: 556 to 6 922 m).

For the wind input source term of our calculation, we used the formulation of exponential growth derived by Komen et al. (1984) with no linear growth item. In addition to the parameters' default values, we used the following specific parameters: 1. boundary conditions by significant wave height reanalysis datasets derived by ECMWF; 2. bottom friction by Jonswap constant of 0.1; 3. numerical accuracy of the significant wave height in iterative calculations by 0.02 (default value, 0.01); 4. numerical accuracy of the fulfilled fraction of all wet grid points in iterative calculations of the significant wave height and the wave period by 98.0 (default value 99.5); and 5. the maximum number of iterations per time step by 15 (default value 1).

Wind forcing and wave boundary conditions are based on data from the European Centre for Medium-Range Weather Forecasts (ECMWF) established in 1975. We selected the data with the horizontal resolution of 0.125° and time interval of 6 hours. The U and V components of the 10-m wind speed are used to drive the SWAN model. The wind components with a resolution of 0.125° were linearly interpolated onto the model grid. To involve the swells from the outer ocean, we also used the ECMWF data at the open boundaries.

Table 2 Instrument locations and information provided for model calibration

Instrument name	Location	Wind speed (m/s)	Longitude, latitude	Time	Depth (m)	Parameters provided	Time interval
Buoy	Batemans Bay	Up to 11	150.336 9°E, 35.707 7°S	10–29 Oct. 2009	55.7	H_s	1 h
Buoy	Sydney	Up to 14	33.768 9°E, 151.441 9°S	10–29 Oct. 2009	93.9	H_s	1 h
ADPDeployment1	Site B in Jervis Bay	<7	150.755°E, 35.113 2°S	18 Mar to 16 Apr 2009	18	u, v, w components	1 s
ADPDeployment2	Site E in Jervis Bay	<8	150.708 2°E, 35.112 7°S	16 Nov to 18 Dec 2009	11	u, v, w components	1 s

2.3 Deployments of ADPs and buoys

Two bottom-mounted ADPs (SonTek 1.5 Mhz) were deployed (Table 2) to measure the high-frequency current velocities. The ADPs were conventionally mounted 1.5 m above the bottom and measured a 1.2-m range of the water column 0.3 m below the ADP (downward-looking), ranging from 0 to 1.2 m from the bottom. Within the 1.2-m range, 26 vertical layers were observed. That is to say, the vertical spatial interval was 0.05 m. The converting coefficient from the bottom to the surface was sinhkh/sinh$k(h+z)$] (see Section 2.2) for the wave departure. Deployment 1 at Site B in JB was at a water depth of 18 m, and deployment 2 at Site E was at a water depth of 11 m. The ADP operated once each hour for 17 min. The time interval of velocity sampling is 1 s. The locations of Sites B and E are denoted in Fig.1c with red diamonds.

The simulated results were validated using data from two wave-rider buoys located at Batemans Bay and offshore Sydney (Table 2), respectively. We selected a period during which the wind speed was greater than 10 m/s because strong wind can validate the prediction of wind-generated waves. The rider buoys of directional waves were used in deep or intermediate-depth water. The water should be deep enough to minimise wave refraction, diffraction, shoaling and friction attenuation effects. The directional wave rider in Batemans Bay was at a water depth of 55.7 m, and the directional wave rider near Sydney was at a water depth of 93.9 m. The deployment positions of the buoys are marked with red diamonds in Fig.1b. We selected 457 h for model validation, starting from 10:00 (Australia Eastern Standard Time) 10 Oct. 2009 (Fig.3).

3 RESULT

3.1 SWAN calibration by buoy observation in strong winds

Figure 3 shows the time variation of the significant wave height (H_s) in Batemans Bay and Sydney. The buoy observations and SWAN simulation match well, except that the SWAN model cannot achieve the highest H_s of 4.5 (Fig.3a) and 6.0 m (Fig.3b) during a surge at wind speeds of 12 (Fig.3e) and 14 m/s (Fig.3f). Figure 3g and 3h show that the model results can predict wind-generated waves well.

3.2 Model validation based on ADP-derived H_s

Figure 4a and 4e contains 120 dots of comparison between the model and the observations, and Fig.4b and 4f comprises 65 comparison data points. To account for the temporal variations, Fig.4a–d illustrate that the simulated H_s values match the ADP observations under moderate wind conditions, whilst the ADP-derived H_s values are sharper and show greater oscillation than the model values in high wind conditions. The ADP analysis results more closely approached the tendency of wind speed variety than the SWAN model (Fig.4c and 4d). Figure 4e and 4f describe the contrast scatter of observations and simulations.

Figure 4g Taylor diagram shows that the precision of simulated T_p is not as good as H_s. The correlation coefficients of T_p are around 0.6, whilst the coefficients of H_s at Sydney and Batemans Bay are between 0.9 and 0.95. The standard deviations (STD) of H_s at Site E and Site B are 0.285 and 0.121 m, respectively. The root mean square difference error (RMSE) of H_s at Site E and Site B are 0.255 and 0.098 m.

We carefully determined the cut-off frequency (Fig.5c and 5d) of the spectra one by one to exclude noise that did not belong to waves (e.g., tidal current or turbulence). We removed the tails at low and high frequencies that mask the spectra of the actual interest.

Two moments at Site B and Site E, respectively, were chosen to display the largest spectra (Fig.5) obtained from the ADP. The selection range of radian frequency was 0.34 to 0.96 at site B, whilst the selected radian frequency was 0.4 to 1.33 at Site E. Figure 5 shows that the peak frequency was about
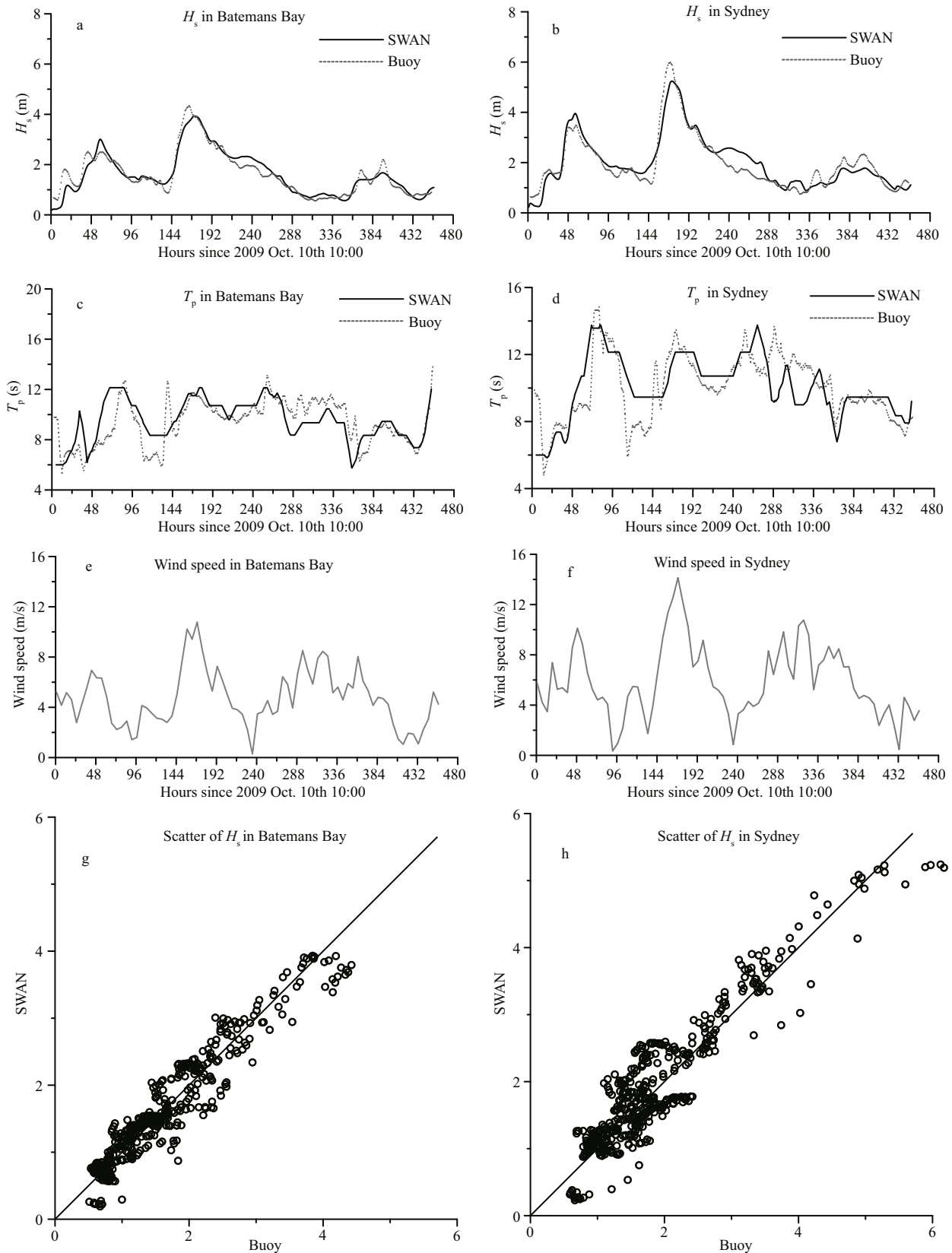
Fig.3 Time series of significant wave height (H_s) for buoys in Oct. 2009 in Batemans Bay (a) and Sydney (b). Data are given in metres; corresponding time series of peak wave period (T_p) speed (c and d). Data are given in seconds; corresponding time series of wind speed. Data are given in metres per second (e and f); scatterplots of H_s data from buoys and SWAN in Oct. 2009 in Batemans Bay (g) and Sydney (h)
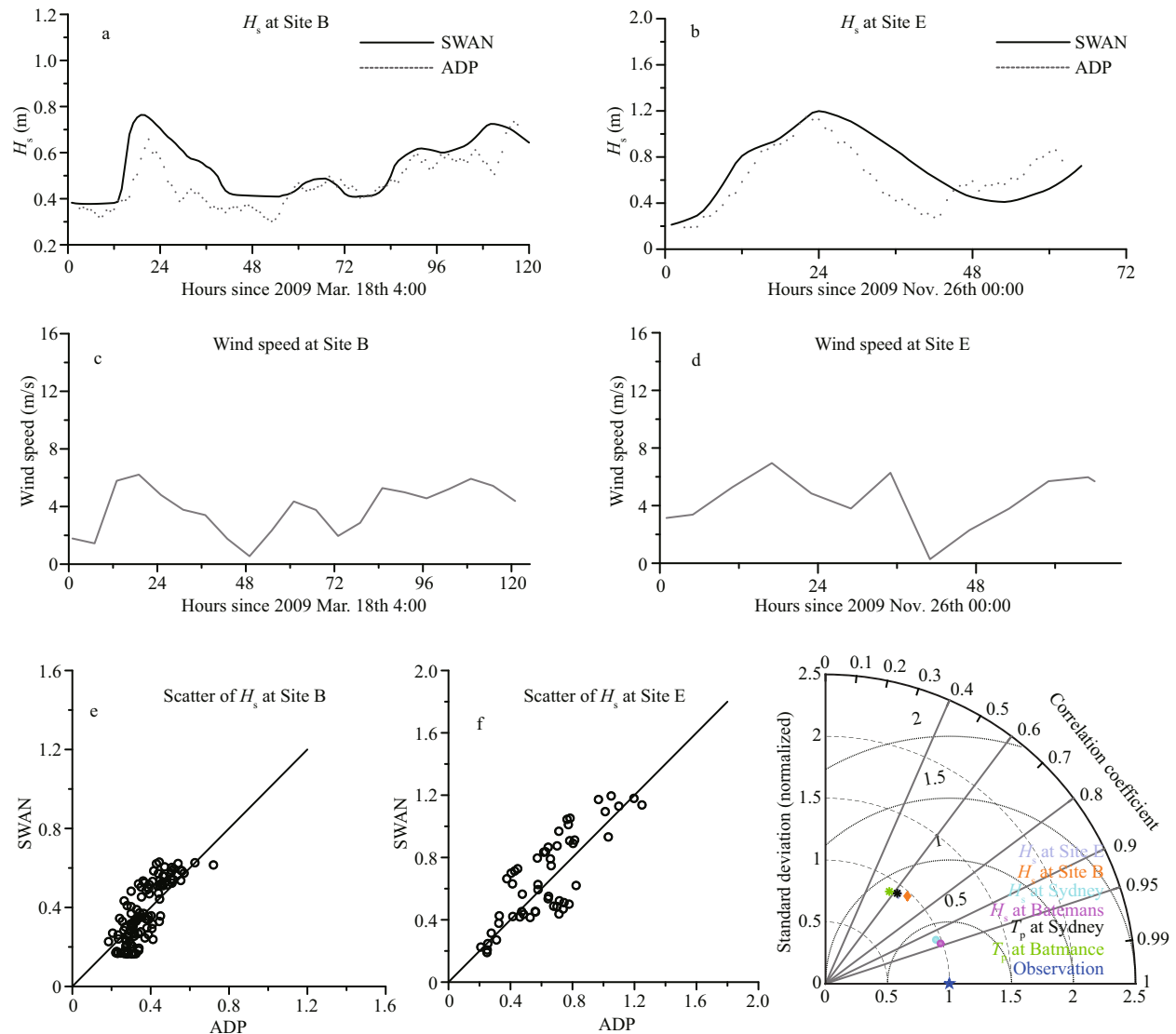
Fig.4 Time series of ADP-derived (gray dots) and SWAN-simulated (black line) H_s at stations B (a) and E (b), and the corresponding wind speeds at the two stations (c and d); scatterplots of H_s data derived from ADP and SWAN simulation at the two stations (e and f);. Taylor diagram (g)

Error statistics contain the H_s at Site B, Site E, Sydney and Batemans Bay and the wave period at Sydney and Batemans Bay. The root mean square error (RMSE) and standard deviations (STD) here are normalised (divided by STD of the observations).

0.1 Hz, which means that the peak period (T_p) was 10 s. This sort of T_p belongs to swells. The wind speed was 5 m/s, and wind of this strength can hardly generate wind waves locally. The peak spectra are 0.15 and 0.8 m^2/Hz in Fig.5a and 5b, which correspond to 0.6 and 1.4 m (peak H_s) in Fig.4a and 4b, respectively.

During the time of ADP observation, the derived spectra and wind speeds were used to distinguish wind-generated waves and swells. Figure 6 presents the relationship of the dimensionless $\tilde{m}$ (y axes in Fig.8, Eq.8) to dimensionless $\tilde{f}_m$ (x axes in Fig.6, Eq.9). U is the corresponding wind speed, and $\tilde{m}$ is integrated from wave spectrum (Eq.3).

$$\tilde{m} = \frac{mg^2}{U^4}, \tag{8}$$

$$\tilde{f}_m = \frac{Uf_m}{g}. \tag{9}$$

Figure 6 shows that the waves are not wind-driven but belong to swells, even though the entrance of the bay is narrow. For wind-generated waves, the dependence of the dimensionless wave variance $\tilde{m}$ on the dimensionless peak frequency should be distributed along the straight line of $\tilde{f}_m = 10^0$ to $\tilde{m} = 10^{-2}$.
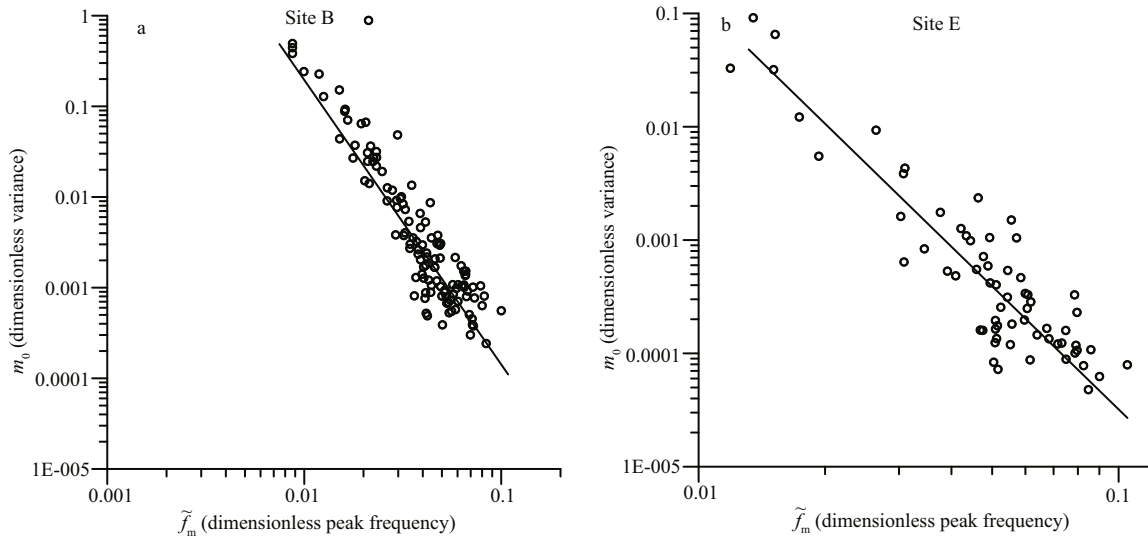
3.3 Characteristics of surface waves in JB

In Sections 3.1 and 3.2, comparisons between the
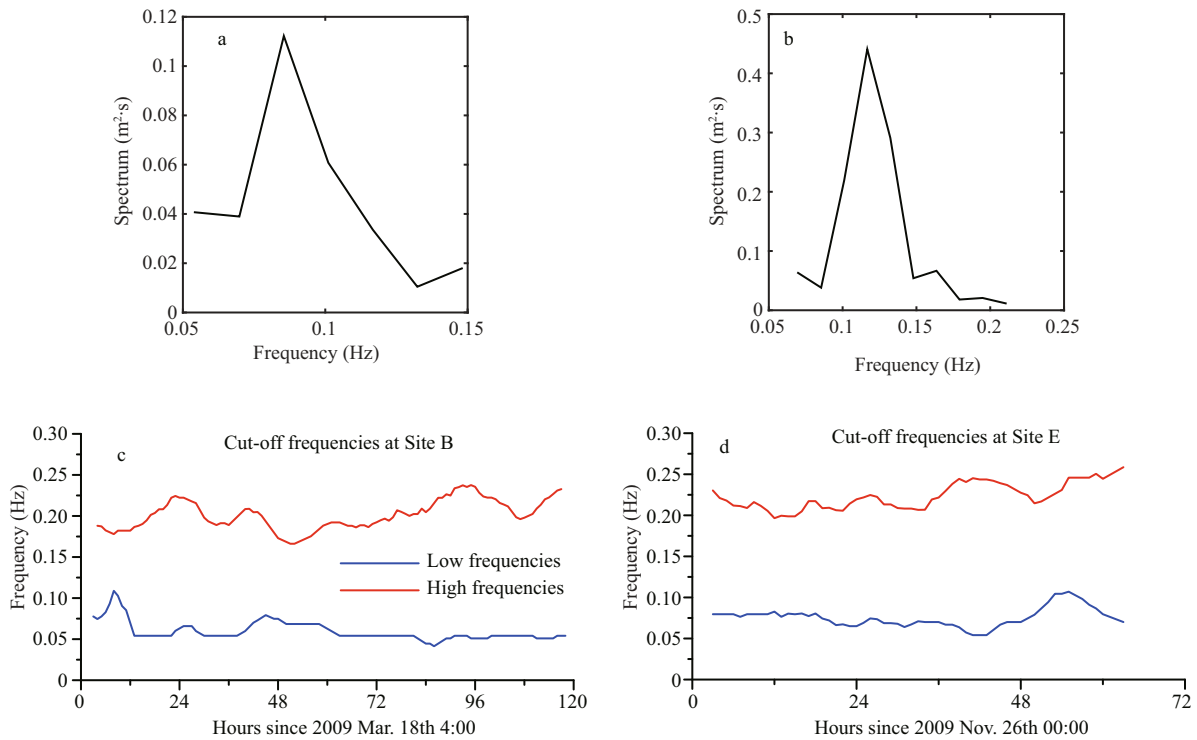
Fig.5 Largest spectra near the bottom obtained from ADPs

a. spectra at site B, at wind speed of 5.7 m/s, at 00:00 19 Mar 2009; b. spectra at site E, at wind speed of 5.2 m/s, at 21:00 26 Nov 2009; c, d. time series of cut-off frequencies of ADP data.


Fig.6 Dependence of dimensionless wave variance $\tilde{m}$ on dimensionless peak frequency f_m Site B (a) and Site E (b) during the ADP's observation time

data from buoys and the SWAN simulation verified the model in both strong and moderate winds. The model could simulate well both the wind-generated waves and the swells. Furthermore, a series of bottom-mounted ADP data at water depths of 11 m and 18 m in JB was used to extract waves in moderate winds in March and November 2009 for model verification.

We averaged four typical months of January, April, July and October to represent all four seasons. We ran the model for the 5 years from 2009 to 2013. Figure 7 shows that the general tendency of H_s decreased from south-east (entrance of the bay) to north-west (top of the bay) throughout the year. The contour lines of the H_s values converge at the bay entrance, which means that these values vary sharply across the bay entrance. The H_s values inside the bay are small, and those
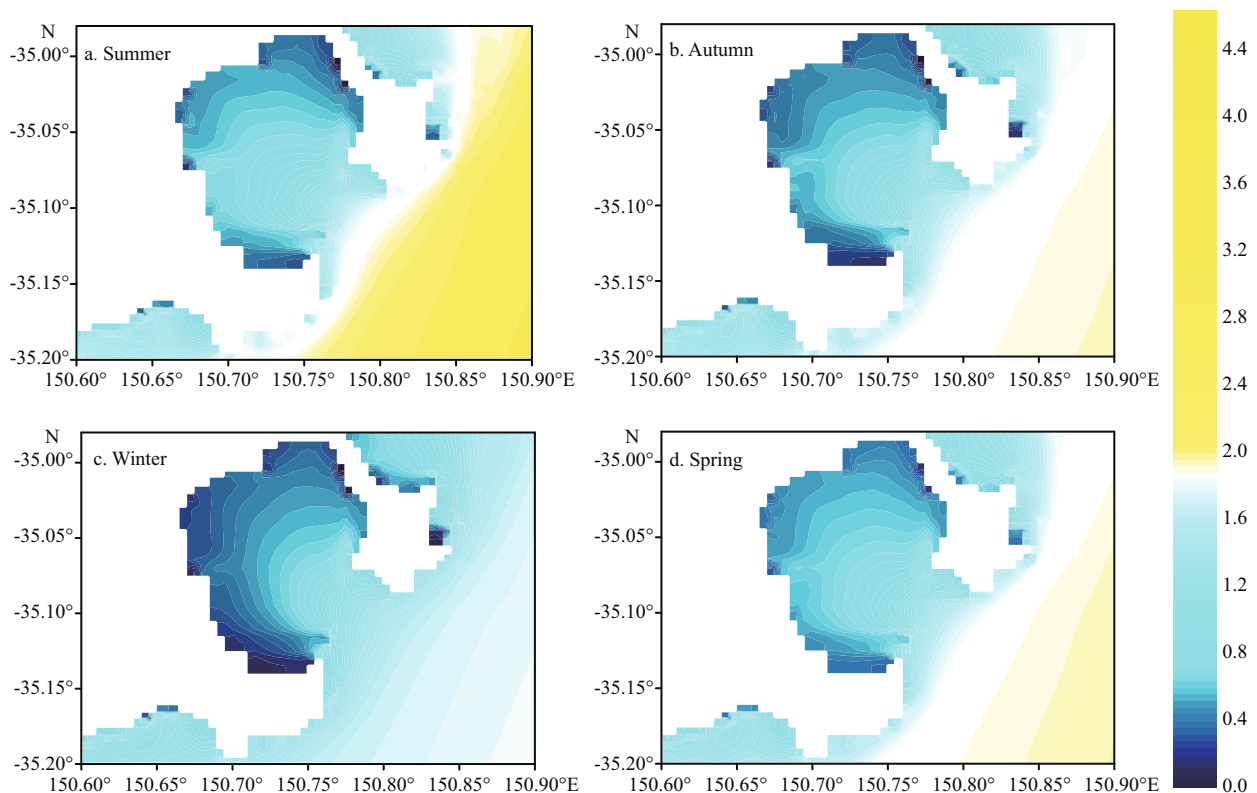
Fig.7 Distribution of H_s in JB

Data are given in metres. a. summer; b. autumn; c. winter; d. spring.

outside the bay are large. The H_s values were less than 1 m/s inside the bay and about 1.2 m at the bay mouth. The H_s values show a correlation with water depth (see Fig.1c). The H_s is roughly 0.4 to 0.6 m where the water depth is shallower than 20 m, and in the middle of bay where the water depth is deeper than 20 m, the H_s varies from 0.6 m to 1 m.

With regard to seasonal variation, the H_s values reach their peak during summer, whilst the minimum value appears in winter. Figure 7b in autumn and Fig.7d in spring show the distribution of H_s values, indicating the transitional traits between summer and winter.

The wave direction in the research area is approximately clockwise (marked by grey vectors in Fig.8) throughout the year. With regard to seasonal variation, swells enter the bay from the northern deep ocean in summer, whilst swells from the south-east area propagate into the bay in winter. The wave direction (Fig.8) near the eastern boundary is south-easterly (in the north) in summer but north-easterly in winter. Correspondingly, along the coastline, the wave direction is south-easterly in summer but south-easterly by easterly in winter. The wave directions in autumn and spring appear to assume a transitional

status between winter and summer. The T_p value in autumn is the largest (Fig.8b) among the four seasons.

Figure 9 shows that the T_p is quite related to the wave direction in JB. The main direction is south-easterly from the bay entrance to the north-west top of the bay, except that the wave direction is south-easterly by easterly in winter. This main direction path separates the wave distribution into two parts— the south-west part and the north-east part. The wave direction is anticlockwise in the south-west part and clockwise in the north-east part. The T_p is high along the main direction line, but low for the other two parts. The T_p in the south-west part with an anticlockwise direction is the smallest of the whole bay (4 to 7 s). The largest T_p appears along the north-west coast of JB, with maxima of 10 s in autumn.

We chose Site A (150.810 0°E, 35.1300 0°S) near the bay entrance to analyse the wave direction. The rise in waves in summer (Fig.9e) shows that the main wave direction is south-easterly, whilst it is easterly in winter (Fig.9g). The rise in wind in summer (Fig.9f) shows that the two dominant wind directions are north-easterly and south-easterly, whilst it is south-westerly in winter (Fig.9h). The differences in the wind and wave directions illustrate that more swells
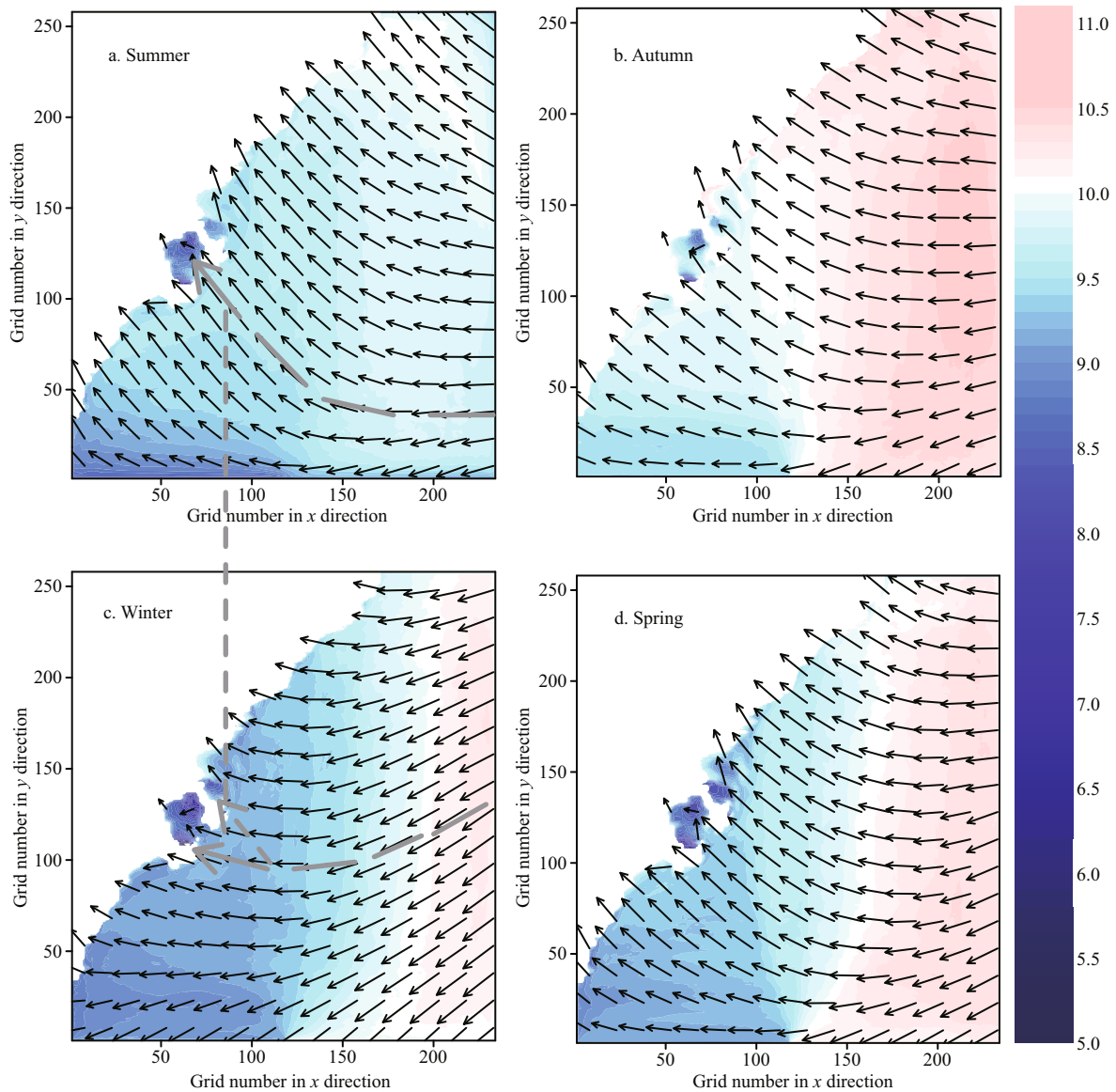
Fig.8 Wave direction overlying relative peak period T_p in the whole model domain, with JB locally zooming in

x and y axes are grid numbers. Data are given in seconds. a. summer; b. autumn; c. winter; d. spring. Wave vector in dashed line of (c) has the same direction as the vector in (a), which means that an angle exists between the wave directions.

are present in JB than sea waves, especially in winter.

To sum up the seasonal variation, both H_s and T_p in JB reach their minimum value in winter, whilst the maximum H_s appears in summer and the largest T_p occurs in autumn. The swell enters JB from the north-eastern ocean in summer, whilst the swell from south-east area propagates into JB in winter. The minimum T_p (and H_s; see Fig.8) in winter is related to the wave direction. The south-west region with an anticlockwise direction is smaller in area, and the period reaches its lowest value of 4 s in winter. Correspondingly, the north-east region with a clockwise wave direction is smaller in area in summer. (An explanation can be seen in Section 4.2).

4 DISCUSSION

4.1 Method of ADP data analysis

When analysing the ADP data, it is acceptable to use a flat-bottom approximation. The linear wave theory is used for cases with infinite depth. Although the conditions are transitional, the bottom slope (Fig.1d) is small and rather uniform. The slope at Site E (11 m) is 0.016 95, and the slope at Site B (18 m) is 0.011 53. Therefore, the small slope makes it reasonable to use the linear wave theory, which is based on a flat-bottom approximation.

However, the converting coefficient from near the bottom to the surface is quite sensitive to water depth
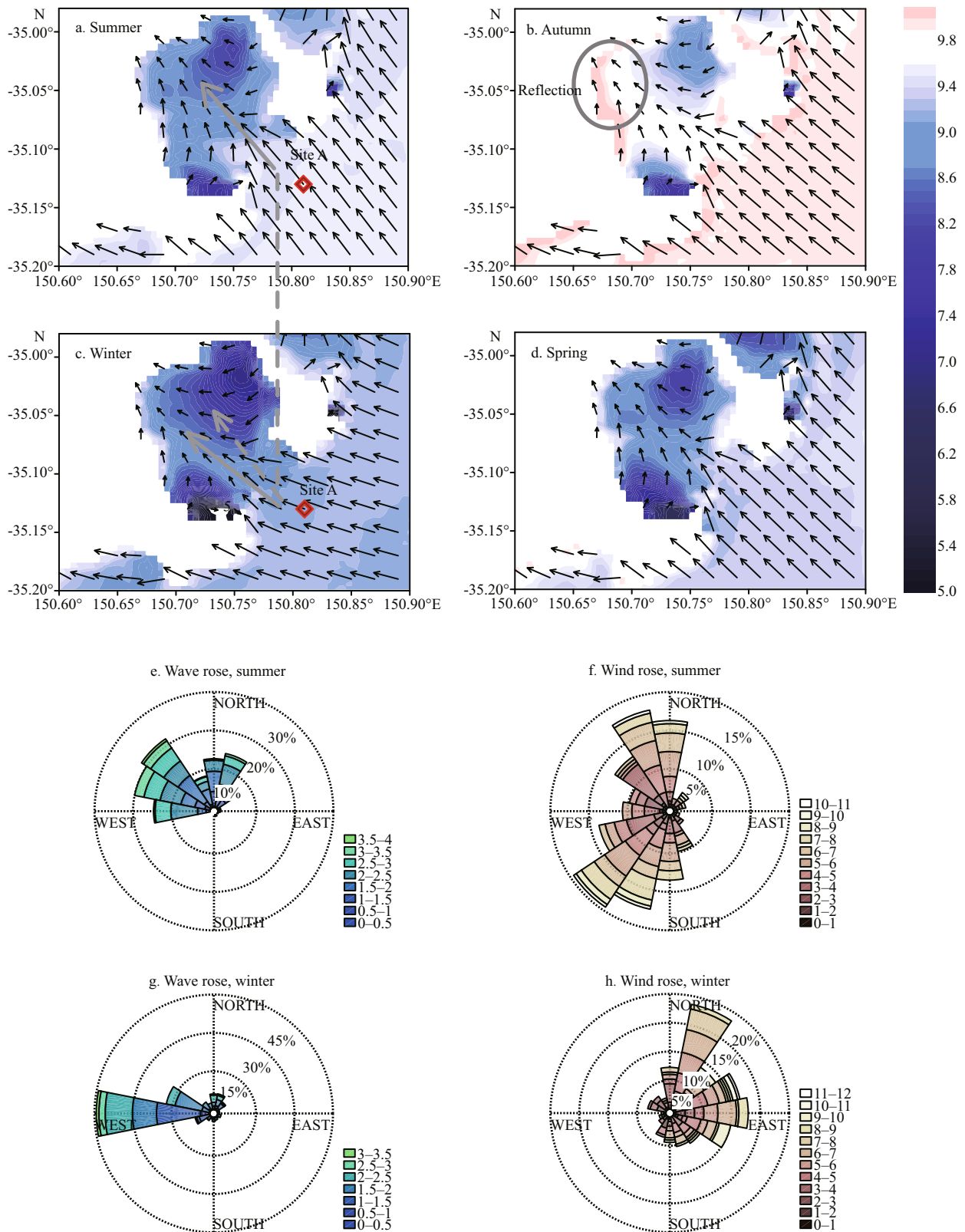
Fig.9 Wave direction overlying wave period T_p in JB

Data are given in seconds. a. summer; b. autumn; c. winter; d. spring. Direction of wave vector in dashed line of (c) is the same as that of the vector in (a), which means that an angle exists between the wave directions. The circle marks the coastal area with large T_p; e–f. wave/wind roses at Site A denoted in (a) and (c); e. wave rose in January; f. wind rose in January; g. wave rose in July; h. wind rose in July. The directions in (e)–(h) represent the waves or winds go to.
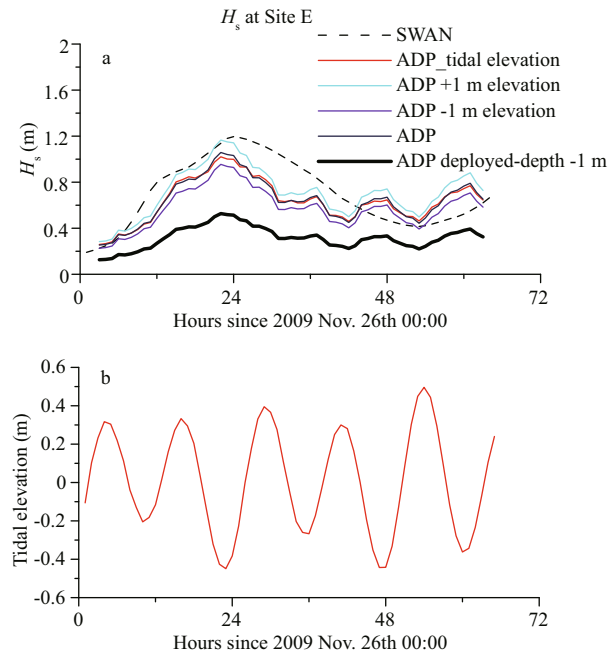
Fig.10 Time series of ADP-derived H_s at Site E in different elevations and ADP depth (a); simulated tidal elevation from POM model (b)

at which the ADP is mounted, but is less sensitive to the water level. As a result, the ADP's mounted depth should be measured precisely to improve the accuracy when converting the bottom spectrum to the surface. We plotted ADP-derived H_s under different elevations (Fig.10). For the water depth of 11 m at Site E, 1 m elevation could result in 0.15 m changes of H_s when the H_s is 1.1 m. If we use the same data but set the deployed-depth 1 m lower (lift the ADP up), the derived H_s will be 0.5 m smaller when the H_s is 1.1 m.

The spectral distribution in strong winds is usually sharper than that in a normal wind, and it is easier to distinguish from currents of other frequencies. The spectrum does not always have a regular distribution. Therefore, the selection of a cut-off frequency should be made carefully to exclude noise from tidal current and turbulence.

PUV method is usually superior to UVW because pressure can be used to adjust the spectrum. The PUV method compares velocity and pressure time series. PUV is a method to obtain wave directional spectra. We used the spectrum $S(\omega)$ rather than directional spectrum $S(\omega, \theta)$. Here, directional wave spectrum is

$$S(\omega, \theta)=H(\omega, \theta)S(\omega), \qquad (10)$$

in which $H(\omega, \theta)$ is function of directional wave propagation.

Our ADPs measured the bottom rather than the surface. It is difficult to directly transform spectrum

from bottom to surface. If we first transform each variable (U, V, W, P) separately from bottom to surface by applying linear wave theory, and then the transformed surface U, V, W and P are used to calculate surface spectrum, the errors could be amplified by this procedure. Our transforming method first calculate the bottom spectrum to get the wave departures. The, we only transform bottom departures to the wave height at the surface. Therefore, the errors are relatively small. Our transforming method mainly discusses the wave departures (Mellor, 2013) near the bottom and the surface wave height.

4.2 Comparisons and explanations for SWAN results

Both the simulated wave direction and the position (south-east) of the bay's entrance are attributed to the wave distribution in JB. The reasons lie in both swells and wind-generated waves as follows. When the wave direction is south-easterly, the barrier effect is low for swell spreading. With the south-easterly trade wind, the fetch can be long enough for local waves to grow. In addition, the reason for the south-easterly wave direction is that the waves become perpendicular to the coastline, stretching from south-west to north-east.

The minimum wave period T_p in winter is related to the wave direction. The period in winter is lowest, although the T_p in the outer ocean is the lowest in summer. This reason for this phenomenon is that the wave direction is south-easterly by easterly in winter and south-easterly in summer. The wave direction in winter is closer to easterly than those of the other seasons. Therefore, less swell can propagate into the bay in winter due to the south-east position of the bay entrance. In summer, the swells can reach the north top of the entrance, whilst swells can only arrive at the west coast of the bay in winter. As a result, the south-west part with an anticlockwise direction is smaller in area in winter, and the T_p reaches its lowest value for the whole year. With regard to the seasonal variation, the swell enters the bay from the northern deep ocean in summer and from the south-east area in winter.

5 CONCLUSION

A SWAN model with a curvilinear grid system was constructed to study wave features near the south-east coast of Australia. This model was verified to predict wave elements effectively by comparing buoy and ADP-derived measurement data. During a strong wind, the model is verified with buoy measurements in Batemans Bay and Sydney.

5.1 Method of deriving wave parameters from ADP measurements

Because the ADP is usually set near the bottom, we deduced a coefficient $\eta = \dfrac{\sinh kh}{\sinh k(h+z)} s_z$ to convert the current velocity near the bottom to the surface wave height. The conversion process is based on the Fourier transform technique and linear wave theory. The converting coefficient from near the bottom to the surface is quite sensitive to the water depth at which the ADP was mounted but less sensitive to the water level.

5.2 Position of bay entrance dominating wave distributions

The south-east position of the bay entrance contributes to the swells' ability to move into the semi-enclosed bay. The waves are not wind-driven but belong to swells, even though the entrance of the bay is narrow. The wave direction is usually south-easterly, and coincidently the entrance to JB is in its south-east part. Therefore, with contribution from the south-easterly waves and the south-east position of JB's mouth, the waves from outer ocean can easily propagate into JB, although the narrow bay mouth can prevent, to a degree, part of the outer swell from propagating into the bay. As a result, the H_s value inside JB is small, and it varies sharply across the bay entrance. The swell enters JB from the north-eastern ocean in summer, whilst the swell from south-east area propagates into JB in winter.

5.3 Relationship between wave period and direction

The wave period T_p is quite associated with the wave direction in JB. The main direction is south-easterly from the bay entrance to the north-west top of the bay. This main path divides the wave distribution into two parts. The wave period is sufficiently large along the whole direction path from the bay entrance to the top of the bay. The T_p value is large along the propagating direction, but small for the other two parts. The wave direction is anticlockwise in the south-west part, but clockwise in the north-east part. The largest T_p value appears along the north-west coast, which is at the end of wave propagation.

6 DATA AVAILABILITY STATEMENT

1. The wind-driven and wave boundary data used to model this study have been downloaded from the ECMWF website: http://apps.ecmwf.int/datasets/data/interim-full-daily/levtype=sfc/;

2. The ADP and buoy data used to support the study's findings were obtained from the University of New South Wales (UNSW), Canberra. These data are available upon reasonable request and with the permission of UNSW.

7 APPENDIX

The detailed procedure to obtain Eq.5 is as follows. Equation 5 is obtained from $\dfrac{\partial s_z}{\partial t} = w = \dfrac{\partial \phi}{\partial z}$, in which the wave potential ϕ is $\phi = \dfrac{a\sigma}{k}\dfrac{\cosh k(z+h)}{\sinh(kh)}\sin(kx - \sigma t)$ as in the linear wave theory. We then have

$$\frac{\partial s_z}{\partial t} = w = \frac{\partial \phi}{\partial z} = \frac{a\sigma}{k} k \frac{\sinh k(h+z)}{\sinh kh}\sin\psi$$

$$s_z = a\sigma \frac{\sinh k(h+z)}{\sinh kh}\int \sin\psi\,\mathrm{d}t$$

$$s_z = a\sigma \frac{\sinh k(h+z)}{\sinh kh}\left(-\frac{1}{\sigma}\right)\int \sin\psi\,\mathrm{d}(kx-\sigma t)$$

$$s_z = a\sigma \frac{\sinh k(h+z)}{\sinh kh}\left(-\frac{1}{\sigma}\right)(-\cos\psi). \tag{11}$$

As $\eta = a\cos\psi$, we obtained $s_z = \dfrac{\sinh k(h+z)}{\sinh kh}\eta$ from Eq.11. Therefore, Eq.5 can be acquired, which means that F_{ss} is the transferring coefficient between the surface elevation η and the elevation in the water s_z. Here, ψ represents $\psi = kx - \sigma t$.

8 ACKNOWLEDGMENT

References

Booij N R, Ris R C, Holthuijsen L H. 1999. A third-generation wave model for coastal regions: 1. Model description and validation. *Journal of Geophysical Research*: *Oceans*, **104**(C4): 7 649-7 666.

Chen P, Yin Q H, Huang P. 2015a. Effect of non-Gaussian properties of the sea surface on the low-incidence radar backscatter and its inversion in terms of wave spectra by an ocean wave spectrometer. *Chinese Journal of Oceanology and Limnology*, **33**(5): 1 142-1 156.

Chen Z B, Zhang B, He Y J, Qiu Z F, Perrie W. 2015b. A new modulation transfer function for ocean wave spectra retrieval from X-band marine radar imagery. *Chinese Journal of Oceanology and Limnology*, **33**(5): 1 132-1 141.

Churchill J H, Plueddemann A J, Faluotico S M. 2006. Extracting Wind Sea and Swell from Directional Wave Spectra Derived from a Bottom-Mounted ADCP. WHOI-2006-13, https://doi.org/10.1575/1912/1372.

Komen G J, Hasselmann K, Hasselmann K. 1984. On the existence of a fully developed wind-sea spectrum. *Journal of Physical Oceanography*, **14**(8): 1 271-1 285.

Mellor G. 2013. Pressure-slope momentum transfer in ocean surface boundary layers coupled with gravity waves. *Journal of Physical Oceanography*, **43**(10): 2 173-2 184.

Pallares E, Sánchez-Arcilla A, Espino M. 2014. Wave energy balance in wave models (SWAN) for semi-enclosed domains—application to the Catalan coast. *Continental Shelf Research*, **87**: 41-53.

Pinkel R, Smith J A. 1987. Open ocean surface wave measurement using Doppler sonar. *Journal of Geophysical Research*: *Oceans*, **92**(C12): 12 967-12 973.

Rorbaek K, Andersen H. 2002. Evaluation of wave measurements with an acoustic Doppler current profiler. *In*: OCEANS 2000 MTS/IEEE Conference and Exhibition. IEEE, Providence, RI, USA. **2**: 1 181-1 187.

Siadatmousavi S M, Allahdadi M N, Chen Q, Jose F, Roberts H H. 2012. Simulation of wave damping during a cold front over the muddy Atchafalaya shelf. *Continental Shelf Research*, **47**: 165-177.

Siadatmousavi S M, Jose F. 2015. Winter storm-induced hydrodynamics and morphological response of a shallow transgressive shoal complex: northern Gulf of Mexico. *Estuarine*, *Coastal and Shelf Science*, **154**: 58-68.

Signell R P, Carniel S, Cavaleri L, Chiggiato J, Doyle J D, Pullen J, Sclavo M. 2005. Assessment of wind quality for oceanographic modelling in semi-enclosed basins. *Journal of Marine Systems*, **53**(1-4): 217-233.

Strong B, Brumley B, Terray E A, Stone G W. 2000. The performance of ADCP-derived directional wave spectra and comparison with other independent measurements. *In*: OCEANS 2000 MTS/IEEE Conference and Exhibition. IEEE, Providence, RI, USA. **2**: 1 195-1 203.

SWAN Team. 2014. Scientific and Technical Documentation. SWAN cycle III version 41.01. Delft University of Technology, Delft, the Netherlands. 126pp.

Wright L D. 1976 Nearshore wave-power dissipation and the coastal energy regime of the Sydney-Jervis Bay region, New South Wales: a comparison. *Australian Journal of Marine and Freshwater Research*, **27**(4): 633-640.